

Reconstruction, rumpling, and Dirac states at the (001) surface of a topological crystalline insulator $\text{Pb}_{1-x}\text{Sn}_x\text{Se}$

A. Łusakowski and P. Bogusławski
*Institute of Physics, Polish Academy of Sciences,
Al. Lotników 32/46, PL-02-668 Warsaw, Poland*

T. Story
*Institute of Physics, Polish Academy of Sciences,
Al. Lotników 32/46, PL-02-668 Warsaw, Poland*
and
*International Research Centre MagTop,
Institute of Physics, PAS, Al. Lotników 32/46,
PL-02-668, Warsaw, Poland*

Equilibrium atomic configuration and electronic structure of the (001) surface of IV-VI semiconductors PbTe, PbSe, SnTe and SnSe, is studied using the density functional theory (DFT) methods. At surfaces of all those compounds, the displacements of ions from their perfect lattice sites reveal two features characteristic of the rock salt crystals. First, the ionic displacements occur only along the direction perpendicular to the surface, and they exhibit the rumpling effect, *i.e.*, the vertical shifts of cations and anions differ. Second, the interlayer spacing of the first few monolayers at the surface oscillates. Our results are in good agreement with the previous X-ray experimental data and theoretical results where available. They also are consistent with the presence of two {110} mirror planes at the (001) surface of the rock salt. On the other hand, experiments performed for the topological $\text{Pb}_{1-x}\text{Sn}_x\text{Se}$ alloy indicate breaking of the mirror symmetry due to a large 0.3 Å relative displacement of the cation and anion sublattices at the surface, which induces the opening of the gap of the Dirac cones. Our results for $\text{Pb}_{1-x}\text{Sn}_x\text{Se}$ including the simulated STM images, are in contradiction with these findings, since surface reconstructions with broken symmetry are never the ground state configurations. The impact of the theoretically determined surface configurations and of the chemical disorder on the surface states is analyzed.

I. INTRODUCTION

Various propositions envisioned for applications of topological materials rely on control of their electronic structure. This issue is motivating a considerable ongoing experimental and theoretical research. As it was demonstrated, properties of topological electron states can be tuned by gate voltage, crystal strain, magnetic field, or magnetization. This includes in particular the opening of the energy gap in the otherwise metallic Dirac-like spectrum.

In the case of the IV-VI narrow gap semiconductors $\text{Pb}_{1-x}\text{Sn}_x\text{Te}$ and $\text{Pb}_{1-x}\text{Sn}_x\text{Se}$ studied here, it is possible to observe a transition from a normal insulator (NI) to a topological crystalline insulator (TCI) phase by changing chemical composition, external pressure, or temperature. Those materials crystallize in the rock salt (*rs*) structure.^{1,2} The key physical factor responsible for the existence of the nontrivial topological phase is not the time reversal symmetry, as is the case of well known topological insulators $(\text{Bi,Sb})_2(\text{Te,Se})_3$, but the mirror symmetry with respect to the {110} crystallographic planes [3–6]. This symmetry warrants the existence of zero gap Dirac-like states on certain high-symmetry crystal facets of TCI crystals, like (001), (111) or (110).

Scanning tunneling microscopy and spectroscopy (STM/STS) and Landau levels spectroscopy (LLS) experiments suggested that at the (001) surface of

$\text{Pb}_{1-x}\text{Sn}_x\text{Se}$ the anion and cation sublattices are displaced with respect to each other along the [110] direction.^{7,8} Such a displacement preserves the mirror symmetry with respect to the (110), but breaks the symmetry with respect to the $(\bar{1}10)$ plane. This symmetry breaking gives rise to the opening of the gap in two out of total four valleys of surface Dirac TCI states located near the \bar{X} -points of the surface Brillouin zone (projections of four bulk *L*-points) on $\bar{\Gamma}-\bar{X}$ lines. Recently, such a symmetry breaking was also observed in $\text{Pb}_{1-x}\text{Sn}_x\text{Te}$ [9]. The results of STS/LLS studies in magnetic field [7] confirmed the conclusion that two kinds of surface states coexist, those with a vanishing energy gap and those with a finite one. In the subsequent paper [8] the STM images directly showed the relative displacement of sublattices of about 0.3 Å. In both papers, only the low temperature measurements were reported. This problem was also studied experimentally in Ref. [10] by angle-resolved photoemission spectroscopy (ARPES), a technique able to selectively study different valleys in the *k*-space. Importantly, the analysis included samples with different Sn concentrations, and was performed at different temperatures. In agreement with Refs. 7 and 8, at low temperatures two kinds of surface states were observed – gapless and with the energy gap of the order of 25 meV [10]. The surface gap decreased with the increasing temperature and, depending on *x*, it disappeared in the temperature range 100 – 200 K, as expected from the topological $T-x$

phase diagram of $\text{Pb}_{1-x}\text{Sn}_x\text{Se}$.¹¹ In the papers^{7,8,10} the mechanism of symmetry breaking at the surface of bulk crystals with the perfect cubic symmetry was not proposed. Instead, the effect was tentatively ascribed to the tendency of the IV-VI crystals to the transition from the cubic to the rhombohedral phase observed in tellurides SnTe , GeTe , and $\text{Pb}_{1-x}\text{Sn}_x\text{Te}$.^{1,2}

The surface reconstruction proposed in [8] is unexpected. This is because previous theoretical and experimental works on $\{001\}$ surfaces of compounds crystallizing in the rock salt structure^{12–18} revealed that in all cases considerable displacements from the ideal bulk sites take place, but their character is in qualitative disagreement with that found in [8]. In particular, three features universally characterize surface equilibrium geometries^{12–18}. First, atomic displacements occur in the z -direction (perpendicular to the surface) only, thus both the ideal rs surface periodicity and symmetry are maintained. Second, the top surface layer is not ideal flat, because cations and anions shift by different amounts in the z direction; this effect is referred to as rumpling. Third, the average interlayer spacings relative to the ideal bulk geometry are modified, and the distance between the first and the second layer is reduced while that between the second and the third layer is increased compared to the ideal bulk value. Such an oscillatory behavior occurs for the first few subsurface atomic layers. No (110) mirror plane symmetry breaking reconstructions were found. Sawada and Nakamura¹⁶ summarized early works, and used the Verwey model¹⁸ to show that the relaxations are largely determined by electrostatics. In fact, responsible for the effects above are both long range electric fields and different atomic polarizabilities of cations and anions.

Results for $\text{Pb}_{1-x}\text{Sn}_x\text{Te}$ are contradictory as well. Yan *et al.*¹⁹ studied the band structure of $\text{Pb}_{1-x}\text{Sn}_x\text{Te}(111)$ overlayers in the full composition range. The Dirac states were seen by ARPES also for the TCI SnTe , and neither band gap nor crystal structure anomalies were noticed. On the other hand, recently a symmetry breaking analogous to that in $\text{Pb}_{1-x}\text{Sn}_x\text{Se}$ was also observed [9].

Here, we theoretically study the ground state atomic configurations and the electronic structure of the (001) surfaces of some semiconductors from the IV-VI family. Of particular interest are the possible mechanisms of symmetry breaking and the gap opening in surface states. The paper is organized as follows. In Section II we present details of the *ab initio* calculations, together with the method of obtaining the Tight Binding Approximation (TBA) Hamiltonian from the *ab initio* results. Section III is devoted to the geometric optimization of the considered systems. Our results are in full accord with the previous findings^{12–18} regarding the features of surface geometry of the rs crystals listed above, but do not confirm the surface reconstruction proposed in Ref. [8]. An additional insight is obtained from our simple simulations of the STM images. Finally, electron dispersion relations of the surface states are provided, where

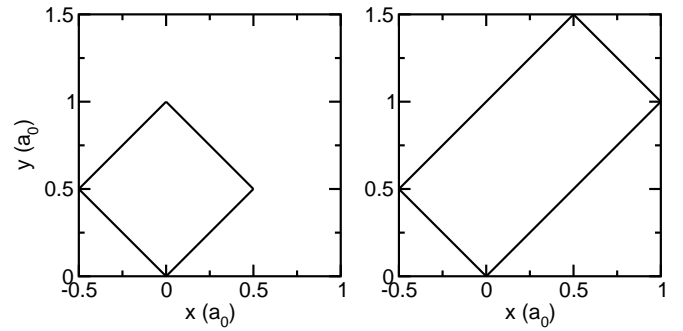


FIG. 1. Surface unit cells for (a) SC1 and SC2 (b) supercells, see text.

we also study the influence of both surface deformations and chemical disorder on the band gap. This allows to determine how a realistic atomic-scale surface morphology of the crystal facets hosting topological states influences electronic spectrum. We identify the conditions under which the Dirac-cone like metallic spectrum can be shifted in the k -space along specific directions, or can exhibit about 1-10 meV gap opening effect relevant, for e.g. FIR and THz applications. Section IV concludes the paper.

II. METHODS OF CALCULATIONS

Properties of layers are analyzed using slabs with the identical top and bottom layers, and thus with the odd number of monolayers. The slabs are separated by 10 Å of vacuum. For pure compounds the supercell SC1 is defined by the vectors $\mathbf{a}_1 = a_0(\frac{1}{2}, \frac{1}{2}, 0)$, $\mathbf{a}_2 = a_0(-\frac{1}{2}, \frac{1}{2}, 0)$ and $\mathbf{a}_3 = a_0(0, 0, n_h + \frac{1}{2})$, where $2n_h + 1$ is the number of monolayers in the slab. The surface unit cell contains one cation and one anion. For mixed crystals, when we want to take into account the symmetry breaking due to chemical disorder, we use larger supercells SC2 based on vectors $\mathbf{a}_1 = a_0(1, 1, 0)$, $\mathbf{a}_2 = a_0(-\frac{1}{2}, \frac{1}{2}, 0)$ and $\mathbf{a}_3 = a_0(0, 0, n_h + \frac{1}{2})$. The supercell SC2 consists of two supercells SC1, what enables an easy presentation of dispersion relations. The surface unit cells of SC1 and SC2 are shown in Fig. 1.

The DFT calculations are performed using OpenMX package.²⁰ They are based on the local density approximation²¹ and the exchange-correlation functional of Ref. [22]. Summations over the Brillouin Zone are performed applying a $4 \times 4 \times 1$ mesh, with the convergence check using a $8 \times 8 \times 1$ mesh for SC1, and $4 \times 8 \times 1$ for SC2. Atomic pseudopotentials for Pb and Te were described in Ref. [23], and those for Sn and Se were taken from OpenMX. Atomic relaxations in the first five surface layers are taken into account. The calculations were stopped when the forces acting on atoms were smaller than 10^{-4} Ha/Bohr, and total energy was converged to within 10^{-6} Ha.

The calculated equilibrium rs lattice parameters a_0 are

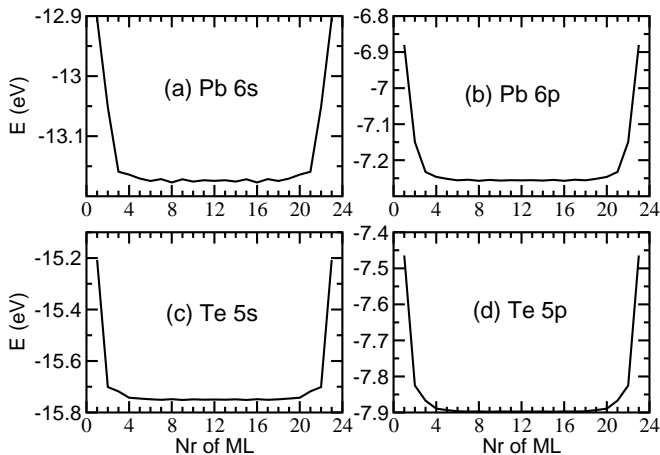


FIG. 2. Calculated dependence of the TBA parameters, namely the energies of the $6s(\text{Pb})$, $6p(\text{Pb})$, $5s(\text{Te})$, and $5p(\text{Te})$ orbitals, on the atomic position in the 23-ML slab.

6.42 Å for PbTe, 6.40 Å for SnTe, and 6.14 Å for PbSe. These values are slightly different from the respective experimental ones which are 6.46 Å, 6.30 Å, and 6.12 Å, respectively. The experimental value for *rs*-SnSe is not known since SnSe in the *rs* structure is unstable, our calculations result in 6.10 Å for *rs* SnSe. Using the theoretical lattice parameters we optimize surface geometry for 11 and 23 monolayer (ML) thick slabs, and the equilibrium atomic positions are practically identical.

Reliable calculations of the dispersion relations of surface states require sufficiently thick slabs. Otherwise, the relevant surface states localized at the top and at the bottom surfaces interact, which leads to a hybridization driven opening of energy gaps in the spectrum of the surface states. Our convergence checks indicate that the coupling between the two surfaces is negligibly small for slabs of the thickness of about 150 ML, in agreement with Ref. [19]. This corresponds to about 600 atoms in the supercell, and thus the *ab initio* calculations, although in principle possible, are nonpractical.

An efficient alternative to apply is the TBA approach based on the LDA results. This requires the knowledge of TBA parameters, and they are provided by the OpenMX code. Here, we use the TBA parameters determined by *ab initio* calculations for 23 ML thick slabs. In the slab geometry, an issue to solve is that the TBA parameters for a given atomic species (*e.g.*, Pb in PbTe) depend on the ion's position in the slab. Indeed, because the local coordination of a Pb ion at the PbTe surface is not the same as in bulk, the parameters of Pb near the surface differ from those in bulk, and this difference depends on the distance from the slab's surfaces. This also holds in the case of the interatomic TBA parameters. According to our results, significant variations of the parameters are limited to 4 ML nearest to surfaces. This important fact was typically ignored in the literature.

As an example, in Fig. 2 we show the dependence of the TBA energies of *s* and *p* orbitals of both Pb and Te ions

on their positions in the PbTe slab. Energy differences between the values in bulk and at the outermost surface layer are 0.3 eV for the Pb orbitals, and somewhat larger, about 0.5 eV, for Te orbitals. The dependencies of the Mulliken charge on atomic positions in the slab, shown in Fig. 3, reveal the same feature: their significant variations are limited to the first four layers. The difference in the values for the first ML and at the slab center is not very large, being of the order of 2 %. Similar differences are found for other TBA parameters, and for the remaining crystals. Importantly however, these variations have a critical impact on the energy dispersion relations and the character of the surface states. This is illustrated in Fig. 4, which presents the dispersion relations for a 123 ML thick slab of PbTe along the $\bar{\Gamma} \rightarrow \bar{X}$ and $\bar{X} \rightarrow \bar{M}$ directions obtained within the TBA. Only the highest 25 valence states and the lowest 25 conduction states are displayed. The bulk lattice parameter $a_0 = 6.20$ Å is assumed, for which PbTe is in the nontrivial topological state.²⁴ The results of the panel (a) are obtained with all TBA parameters equal to the TBA parameters of bulk PbTe. In the case of the panel (b), the TBA parameters are position dependent and determined according to the procedure described below. We expect that the highest occupied levels should be the surface states, and indeed such a situation is observed with a well defined Dirac cross, see the panel (b). In contrast, in the case (a) there is a number of bands above the energy of the highest occupied band, which certainly cannot be classified as conduction bands. We conclude therefore, and this is one of important messages of our work, that the position dependence of the TBA parameters close to the surface must be taken into account.

The position-dependent TBA parameters for thick layers are obtained as follows. We begin with *ab initio* calculations for an easy to handle 23 ML slab with equivalent top and bottom surfaces. The slab is partitioned into

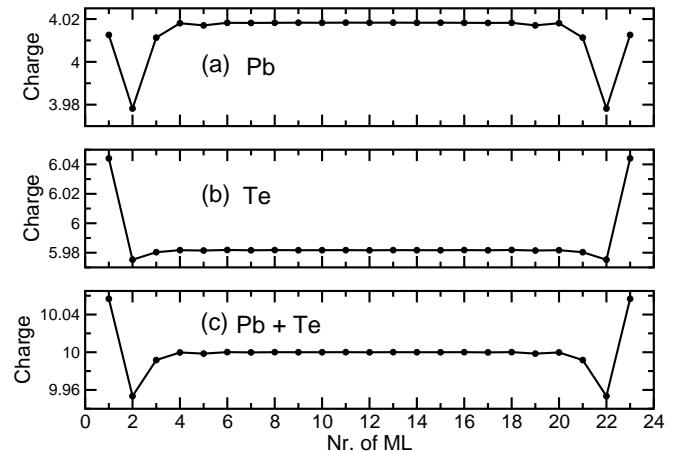


FIG. 3. Dependencies of Mulliken charges on the atom positions in the 23 ML slab: (a) Pb, (b) Te, and (c) the sum of (a) and (b).

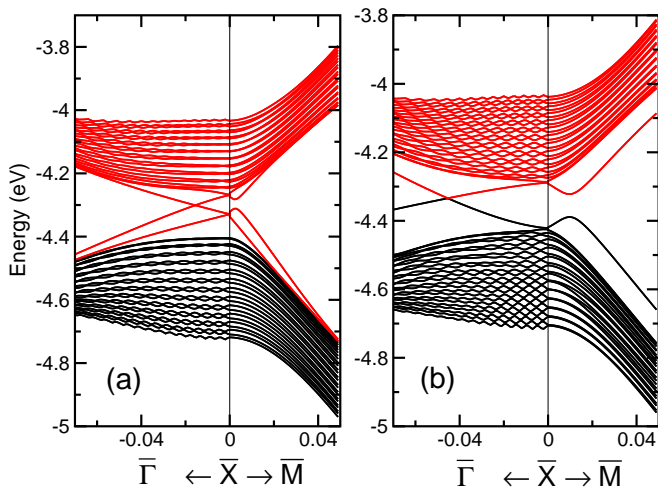


FIG. 4. (color online) Dispersion relations along $\bar{X} \rightarrow \bar{\Gamma}$ and $\bar{X} \rightarrow \bar{M}$ directions of the 25 highest valence (black lines) and the 25 lowest conduction (red lines) bands for 123- monolayer thick slab of PbTe with the lattice parameter $a_0=6.20$ Å. (a) The TBA parameters are independent of the position in the slab, and (b) the TBA parameters are position depended, see text. The wavevector on the x axis along both the $\bar{X} \rightarrow \bar{\Gamma}$ and $\bar{X} \rightarrow \bar{M}$ directions is in the units of $2\sqrt{2}\pi/a_0$.

(III) one, containing 6, 10 and 7 ML, respectively. The corresponding TBA parameters are given in the output of *ab initio* calculations. The assumed thickness of the outer regions I and III guarantees that all surface effects are contained therein, and thus the internal region II reproduces correctly the bulk. In particular, in our TBA method the interatomic couplings extend to the third neighbor of a given atom, and the atomic relaxations along with the effects of the non-bulk coordinations at the surface extend to the first four ML (see Figs 2 and 3). The TBA parameters for the internal region II are those for bulk crystals. Also for thicker slabs three regions are considered. The first and the last regions contain 6 and 7 ML, respectively, and the internal region is a certain number of repetitions of the region II of 23 ML slab. For these three regions the TBA parameters are taken from I, II, and III regions of a 23 thick ML slab, respectively.

III. ATOMIC CONFIGURATIONS AND ELECTRONIC STRUCTURE OF (001) SURFACES

A. Ground state atomic configurations

Atomic configuration at a (001) surface of a rock salt crystal can be defined by two parameters,¹³ namely the average z coordinate of the i -th layer $z(i) = (z_{cat}(i) + z_{an}(i))/2$, and the rumpling parameter of that layer $r(i) = (z_{an}(i) - z_{cat}(i))/d_0$. Here, d_0 is the equilibrium bond length, and the z -coordinate of cations (anions) from the i -th layer with respect to perfect positions is denoted by $z_{cat}(i)$ ($z_{an}(i)$), with $i = 1$ being the sur-

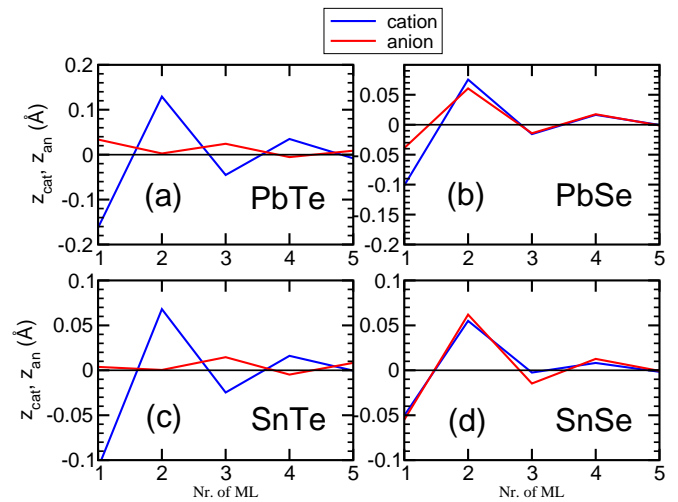


FIG. 5. (color online) Displacements of cations and anions from the ideal rock salt sites in the first 5 monolayers for (a) PbTe, (b) PbSe, (c) SnTe, and (d) SnSe.

face. The change in the interlayer spacing between the layers i and $i + 1$ is $\delta_{i,i+1} = (z(i+1) - z(i))/d_0$. To find the ground state atomic configurations, three initial geometries are considered. In the first one, all atoms are at the ideal rock salt sites. In the remaining cases, the initial displacements for Te atoms are limited to the surface layer only, and amount to (0.3, 0.3, 0) Å and (0.4, 0.2, -0.1) Å, respectively. These choices are meant to initiate the surface configuration suggested in Ref. [8], which breaks the surface symmetry.

We first consider ionic relaxations perpendicular to the surface. The calculated final displacements $z(i)$ along the z axis do not depend on initial configuration, and are shown in Fig. 5 for all the considered compounds. Next, both the rumpling and the interlayer spacing are presented in detail in Fig. 6. For PbTe and PbSe, these parameters were calculated previously.^{12,13,17} There are some differences between our values and those presented in the literature but the qualitative picture is the same. The results for SnSe and SnTe are new to our best knowledge.

The PbTe(001) surface was experimentally investigated in detail. LEED measurements performed in Ref. [12] revealed a large rumpling, $r(1) = 6.8\%$, which corresponds to displacements of about 0.2 Å. Next, the measured interlayer spacings exhibit an oscillatory behavior, with $\delta_{1,2} = 4\%$ and $\delta_{2,3} = -2\%$. Our results shown in Fig. 6 are in a good agreement with these data: the rumpling of the first layer is $r(1) \approx 6\%$, and the changes in interlayer spacings are $\delta_{1,2} \approx 4\%$ and $\delta_{2,3} \approx -2\%$. Previous first principles calculations for PbTe(001)^{12,13,17} found the rumpling somewhat lower than that observed, but they confirmed the outward (inward) shift of Te (Pb) ions. Next, the calculated interlayer spacings exhibited an oscillatory behavior with values close to those measured.

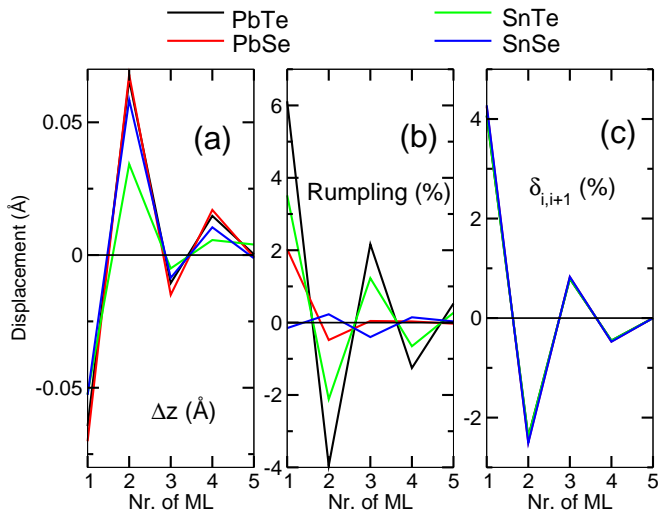


FIG. 6. (color online) Changes of (a) the average z coordinates of the monolayers, (b) rumpling r , and (c) of the interlayer spacings δ for first 5 monolayers of PbTe, PbSe, SnTe and SnSe. Note that the calculated δ s are practically identical for all the considered crystals.

Rumpling in the PbX series depends on the anion. Indeed, in contrast to PbTe(001), a very small rumpling at the PbS(001) surface was observed²⁵. Theoretical results of Refs.^{13,14,17} are in a good agreement with experiment. Interestingly, rumpling at the PbS(001) and PbTe(001) surfaces is opposite, since in the former case the S anions exhibit a small *inward* displacement. According to Fig. 5 and Fig. 6, relaxations at PbSe(001) are intermediate between those for PbS(001) and PbTe(001). In particular, the rumpling at the PbSe (001) is smaller than for

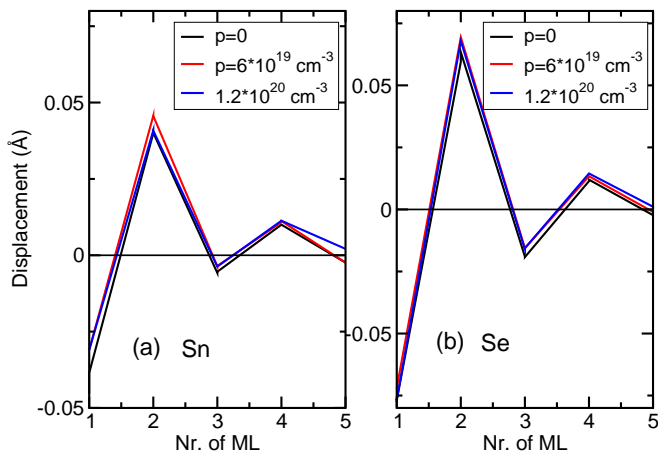


FIG. 7. (color online) Displacements of atoms in the first monolayers of SnSe along the [001] direction with respect to the positions in the perfect rock salt lattice after the geometric optimization as the function of the hole concentration p . The results for Sn and Se are given in Fig. (a) and (b), respectively.

of Ref. [14]. The interlayer spacing exhibits the typical oscillatory behavior.

The results obtained for rs -SnSe and rs -SnTe are presented in Figs. 5 and 6, respectively. As we see, the z -displacements of the consecutive layers are similar for all systems, and the interlayer distances always oscillate. Also the rumpling oscillates, changing the sign for adjacent layers, but it is more pronounced in the tellurides than in the selenides. We recall here that the rs phase of SnSe is only metastable, but nevertheless surface properties of rs -SnSe(001) are expected and found to be similar to those of other members of the rs -IV-VI family.

Equilibrium atomic configurations can depend on the presence of free carriers. Indeed, it is well known that Sn-based IV-VI compounds typically are highly p -type due to the presence of high concentrations of electrically active cation vacancies. This is also the case of crystals investigated in Ref. [8]. There are two possible consequences of this fact. First, charge transfer processes taking place at the surface, see Fig. 3, can be screened and/or affected by the presence of free carriers in the layer. This in turn can influence the surface geometry. Second, bulk SnTe assumes the NaCl structure at higher temperatures, and with the decreasing temperature a transition to the rhombohedral phase takes place. However, this transition is suppressed by concentrations of holes higher than $1.5 \cdot 10^{20} \text{ cm}^{-3}$ [26]. (This transition also becomes suppressed with the increasing content of Pb in $\text{Pb}_{1-x}\text{Sn}_x\text{Te}$) Accordingly, the recent experiment of Wei *et al.*²⁷ suggested that strongly anomalous transport features observed in PbTe/SnTe heterostructures originate in the free-carrier driven symmetry breaking in SnTe layers caused by the above mentioned varying hole densities.

The results above motivated us to analyze the impact of free carriers on atomic displacements. OpenMX package allows performing calculations for nonzero concentrations of free carriers. The calculations were done for free carrier concentrations between 10^{20} cm^{-3} of holes to 10^{20} cm^{-3} of electrons, and the results are shown in Fig. 7. While the relaxation energies (*i.e.*, the energy gains induced by the relaxation from the ideal to the equilibrium configuration) are dependent on carrier concentration to some extent, the final geometries are highly non-sensitive to the presence of free carriers. In all cases, the ionic displacements in the (001) plane are negligibly small. The presence of $1.2 \cdot 10^{20} \text{ cm}^{-3}$ electrons induces ionic displacements of about 0.01 \AA . The same amount of holes induces a similar change, but of opposite sign.

We now turn to the displacements in the (x, y) plane. When the ideal rs configuration is used as input, the final ionic displacements in the (x, y) plane always vanish for all the considered crystals. Using the symmetry-breaking initial configurations leads to final configuration with small displacements of about $|0.03| \text{ \AA}$. We ascribe this result to the finite accuracy of our calculations, since in all cases total energy of the symmetry breaking configurations is higher by about $0.5 \text{ meV}/(\text{surface atom})$ than

that of the symmetric ground state.

Concluding, our results do not confirm the presence of a symmetry breaking in the (x, y) plane at the surface, which were proposed in Ref. [8] based on the STM measurements. In fact, our study indicates instability of those configurations. Also the presence of free carriers can be ruled out as a cause of the surface reconstruction reported in Ref. [8]. Independent experiments, in particular STM, are needed to clarify the situation.

B. Simulation of STM images

Conclusions reported in Ref. [8] regarding the surface geometry are based on the STM measurements. In those measurements the local density of states near the surface plays the main role.²⁸ To make a link with experiment we simulate, in a simplified way, the STM images by calculating the integrated local density of states (ILDOS) $n(\mathbf{r}, E)$ at the distance 1.5 Å from the surface according to

$$n(\mathbf{r}, E) = \sum_{E < \epsilon_{nk} < 0} |\psi_{nk}(\mathbf{r})|^2, \quad (1)$$

where the summation is performed over all electron states with energies ϵ_{nk} belonging to the energy window between E and the top of the valence band (taken as the zero energy). The current in STM measurements is proportional to the ILDOS defined above. In this way, different voltages applied in STM measurements are modeled by different energy windows $\Delta E = -E$. A negative value of E implies that we sum over the occupied valence states, which corresponds to the voltage polarization used in Ref. [8]. The results obtained for PbSe(001) are displayed in Fig. 8 which shows the voltage dependence of STM images. Qualitatively, the figure reproduces the effect presented in Fig. S3 of Ref. [8], and in particular the fact that different atoms are dominant under different STM voltages. In general the anions are more visible because, due to rumpling, the cations are placed deeper in the crystal. However, as expected, the STM images of the symmetric PbSe(001) surface are symmetric as well, and the maxima of the ILDOS $n(\mathbf{r}, E)$ are above the ions.

The simulated STM images change when the surface symmetry is broken, and a relative displacement of the cation and anion sublattices at the surface is assumed. In this case, calculations performed for several surface configurations reveal an interesting effect illustrated in Fig. 9. The images are obtained assuming a lateral displacement of Se in the first ML by $(0.1, 0.1)$ Å and the Se position is shown by a star. On the other hand, the calculated maxima of the electron density occurs at approximately $(0.3, 0.3)$ Å in the case of the very thin slabs of 5 and 9 ML. This result shows that the experimental STM images do not always directly reflect location of atoms at the surface. However, for thicker slabs the effect disappears. Because in Ref. [8] the surface of bulk crystal was studied, STM maxima reflect real positions of atoms.

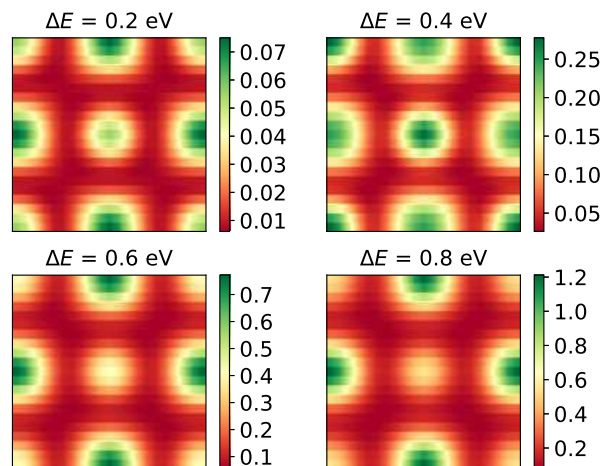


FIG. 8. (color online) Integrated local density of states $n(\mathbf{r}, E)$ at 1.5 Å from the PbSe(001) surface calculated for the varying energy window ΔE counted from the top of the valence band, see text. The figures display the surface unit cell of dimension $a_0 \times a_0$. Pb cations are located at the center and at the corners of the unit cell, and Se anions are at the middle of its edges.

(We mention here that the sensitivity of the PbTe band gap on the slab thickness discussed in Ref. [29] showed pronounced irregularities for a few monolayer slabs. Also, in general atomic configurations suggested by the STM images do not necessarily reflect the actual ones. For example, at the Si(001) surface the apparent tilt of Si dimers is different for positive and negative bias³⁰.)

C. Dispersion relations of surface states. Influence of rumpling

Surface states of the considered systems are affected both by rumpling and by chemical disorder present in alloys. The latter destroys the reflection symmetry with respect to the $\{110\}$ planes. We focus on the two surface states present in the band gap because we are interested mainly in the position of the Dirac cross and the energy gap in the vicinity of the \bar{X} point. Dispersion relations for 133 and 173 ML thick slabs and for $[110]$ and $[\bar{1}10]$ directions are identical.

Figure 10 compares dispersion relations for surfaces of both PbTe and *rs*-SnSe with and without rumpling. The calculations for *rs*-SnSe are done for comparison only because, as we already mentioned, the *rs* phase of SnSe is not stable. In the case of PbTe, the assumed lattice parameter is 6.24 Å for which the compound is in the TCI phase. We see that the rumpling does not lead to opening of the gap at the Dirac cross because the reflection symmetry with respect to the $\{110\}$ planes is not broken. There are two effects induced by rumpling in the vicinity of the \bar{X} point, namely a displacement of the Dirac cross and a change of the energy gap on the $\bar{X}-\bar{M}$ direction.

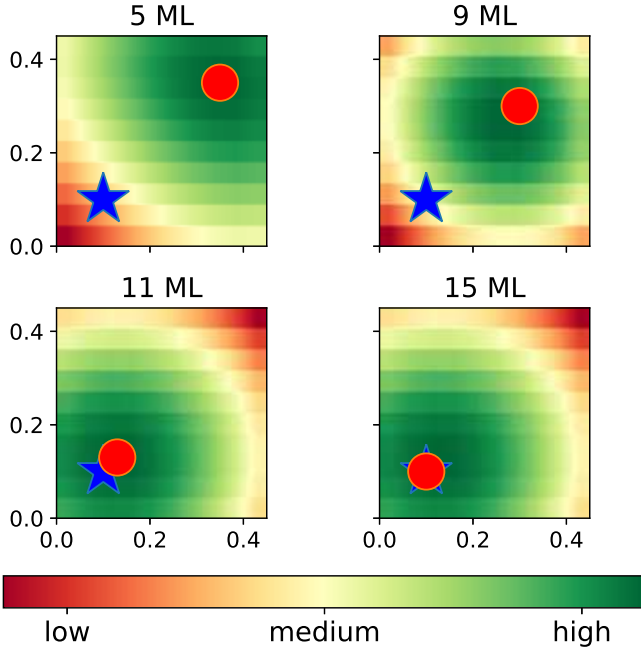


FIG. 9. (color online) ILDOS at the distance 1.5 \AA from the PbSe(001) surface near the displaced Se atom for $E = -0.6 \text{ eV}$. Δx and Δy describe distances relative to the position of Se atom in the perfect rs structure. The actual position of Se is denoted by the blue star, and the maximum of the calculated electron density occurs at the red circle.

Both effects are very small. For rs -SnSe we also observe these two effects, however, compared to PbTe, the shift of the Dirac cross is of opposite sign and the energy gap becomes larger. Similar to the case of PbTe, both effects are small.

D. Bulk chemical disorder

In a pure compound like PbSe, transition from the trivial NI to the TCI phase can be induced by hydrostatic pressure. Since hydrostatic pressure does not change the crystal symmetry, the states at the four L points in the Brillouin zone are degenerate for all values of the lattice constant. Consequently, the transition is sharp, and the band gap changes sign at a well defined value of a_0 .

In alloys, chemical disorder makes the NI-TCI transition more complex. This is because the disorder splits degenerate bands (or it broadens electronic states), and as a consequence the pressure-induced NI-TCI transition is smeared out, *i.e.*, it occurs within a finite window of hydrostatic pressures. In an analogous way, the NI-TCI transition can be induced by changing the chemical composition x of an alloy, but again the band smearing results in a finite composition window in which the band gap vanishes. This was discussed for bulk crystals in Refs 24 and 31. Moreover, it was shown in Ref. [31] that in the transition region the alloy is in the Weyl semimetal

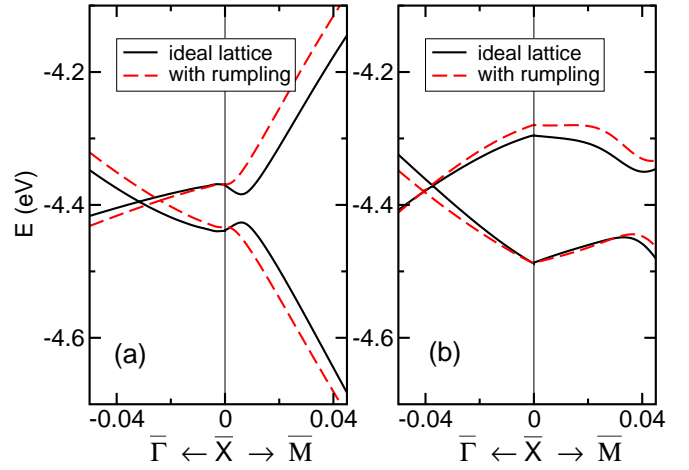


FIG. 10. (color online) The influence of rumpling on the energy bands for (a) PbTe with the lattice parameter $a_0 = 6.24 \text{ \AA}$, when PbTe is in the TCI phase, and (b) rs -SnSe with $a_0 = 6.105 \text{ \AA}$. In both panels only the two surface states present in the band gap are shown. The wavevector on the x axis along both the $\bar{X} \rightarrow \bar{\Gamma}$ and $\bar{X} \rightarrow \bar{M}$ directions is in the units of $2\sqrt{2}\pi/a_0$.

(WSM) phase. Our calculations show that $\text{Pb}_{1-x}\text{Sn}_x\text{Se}$ is in the WSM phase for $0.18 < x < 0.30$, which is close to the window $0.12 < x < 0.30$ obtained in Ref. [31].

In Fig. 11 we present dispersion relations for $\text{Pb}_{1-x}\text{Sn}_x\text{Se}$ 173 ML thick slab with different compositions x and random cation distributions in the supercell. For the lowest content of Sn, $x = 0.15$ (Fig. 11a) the crystal is in the NI phase and the band gap is positive. Detailed analysis shows the splitting of the two lowest conduction and the two highest valence bands at the \bar{X} point. This is a consequence of the chemical disorder

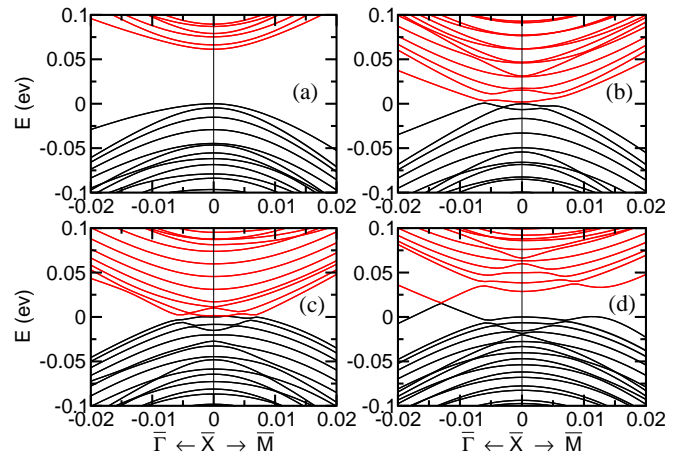


FIG. 11. (color online) Dispersion relations along the $\bar{\Gamma} - \bar{X}$ and the $\bar{X} - \bar{M}$ directions for $\text{Pb}_{1-x}\text{Sn}_x\text{Se}$ with different tin content: (a) $x=0.15$, (b) $x=0.20$, (c) $x=0.25$ and (d) $x=0.30$, respectively. The scales for x axes are in units of the distance between $\bar{\Gamma}$ and \bar{X} points.

and in the case of pure PbSe such a splitting is absent. When $x = 0.3$ (Fig. 11d) the crystal is in the TCI phase, and accordingly the Dirac cross is seen.

Finally, for two intermediate concentrations $x = 0.20$ and $x = 0.25$ (Figs. 11b and 11c) the highest valence bands and the lowest conduction bands overlap in a finite energy interval of a few meV in the vicinity of the \bar{X} point reflecting the impact of the chemical disorder. This is interpreted as a manifestation of the WSM bulk phase.^{24,31}

IV. CONCLUSIONS

The presence and the form of metallic helical Dirac states critically depend on the symmetry of not only a bulk crystal, but also of its surfaces. Here, we study properties of the (001) surfaces of PbTe, PbSe, SnTe and SnSe, as well as of the $\text{Pb}_{1-x}\text{Sn}_x\text{Se}$ substitutional alloy, and pay attention to the possible interplay between the topological TCI phase and the surface geometry. Realistic allocations of atoms in the first few monolayers at the (001) surface are determined by first principles calculations. Equilibrium geometries of all the considered surfaces are typical of the *rs* crystals family. First, the rumpling takes place, *i.e.* cations and anions from the same atomic plane are displaced from the ideal *rs* sites in the z direction perpendicular to the surface. In contrast, ionic displacements in the (x, y) plane of the surface are absent, and therefore the *rs* surface symmetry is not broken. Second, close to the surface, the interlayer distances weakly oscillate. Those features are in agreement with a number of experimental data and theoretical results regarding surface geometries of the IV-VI family and other *rs* crystals. As these effects do not brake the mirror-plane symmetry of the *rs*(001) surfaces, their sole impact on the band structure is to shift the positions of the Dirac points, while opening of the band gap in the spectrum of surface states does not occur. In most cases, the effect of the surface relaxation on the band energies is small, of the order of a few meV. The *rs* symmetry is present also in our simulated STM images of the studied surfaces. On the other hand, a spontaneous symmetry breaking at the (001) surface, accompanied with the band gap opening (destruction of the Dirac cones, and acquisition of mass by surface electrons) were recently reported for $\text{Pb}_{1-x}\text{Sn}_x\text{Se}$ [8] and $\text{Pb}_{1-x}\text{Sn}_x\text{Te}$ [9].

The above discrepancy between experiment and theory requires a comment. Typically, surface reconstructions stem from a specific coordination of surface atoms. An example is formation of dimers at {001} surfaces of zinc blende crystals. An unexpected reconstruction (which we may possibly deal with here) can take place because the film, assumed to be in *e.g.* the *rs* phase, acquires a different crystal structure. Indeed, during the pseudomorphic growth an overlayer adopts the structure of the substrate. When the two structures differ, at some conditions (defined by the critical values of thickness, com-

position, or temperature) the ground state phase of the overlayer overcomes pseudomorphic constraints, and the overlayer changes its structure. Clearly, this results in a change of atomic configurations at the surface as well. With this respect we note that the equilibrium structure of SnSe and $\text{Pb}_{1-x}\text{Sn}_x\text{Se}$ ($x > 0.4$) is orthorhombic,^{32,33} in which phase the (001) surface can acquire the reconstruction pattern claimed in [8] (see Fig. 1 of Ref. [34]). This suggests that a possible source of the observed reconstruction is the onset of the structural bulk instability signaled at the surface. However, one should keep in mind that the observed symmetry breaking is limited to the surface only, since otherwise the band gap would strongly differ from that measured [8].

Second, breaking mirror symmetry leads to formation of surface dipoles [9]. This brings yet another question regarding the surface configuration: experiment reveals one direction of polarization only, while one would expect formation of surface domains with orthogonal orientations of polarization.

Third, in the case of $\text{Pb}_{1-x}\text{Sn}_x\text{Se}$ the details of the reconstruction were directly displayed by the STM images [8]. One can observe, however, an interesting feature exhibited in Fig. S3 of Ref. [8]. Namely, the reconstruction pattern depends on the STM polarization voltage: at about -250 mV the symmetry-breaking mirror plane is (100), which changes to the (110) plane at higher voltages. This effect was not recognized by the authors, and is not reflected in our calculations. Finally, we cannot propose a source of this contradiction. The above remarks are meant to underline the complexity of the issue, and not to question the quoted experimental data.

To study dispersion relations of surface states we use the tight binding approach, with parameters obtained from the DFT calculations. As we demonstrate, it is important to account for the position dependence of the TBA parameters (which differ for ions in the bulk and near the surface), since otherwise the energies of surface states are erroneous. In particular, we analyze the transition from the NI to the TCI phase for the $\text{Pb}_{1-x}\text{Sn}_x\text{Se}$. With the increasing Sn content the alloy undergoes the transition from normal insulator to the Weyl semimetal phase. Because of the disorder induced band broadening, this phase persists in a wide composition window $0.2 < x < 0.3$, in which surface states are characterized by atypical dispersion relations as well as semi-localization at the surface and, eventually, the TCI phase appears for $0.3 < x < 0.4$.

ACKNOWLEDGMENTS

This work was partially supported by National Science Centre NCN (Poland) projects UMO-2016/23/B/ST3/03725 (AŁ), UMO-2017/27/B/ST3/02470 (AŁ) as well as by the Foundation for Polish Science through the IRA Programme

co-financed by EU within SG OP (TS). We thank R. Buczko for helpful discussions.

- ¹ G. Nimtz and B. Schlicht, in: *Narrow-Gap Semiconductors* (ed. G. Höhler), Springer Tracts in Modern Physics, Vol. 98 (ed. G. Höhler) (Springer-Verlag, Berlin 1983).
- ² D. R. Khoklov (ed.) *Lead Chalcogenides: Physics and Applications* (Taylor and Francis, New York 2003).
- ³ T. H. Hsieh, H. Lin, J. Liu, W. Duan, A. Bansil, and L. Fu, *Nature Comm.* **3**, 982 (2012).
- ⁴ P. Dziawa, B. J. Kowalski, K. Dybko, R. Buczko, A. Szczerbakow, M. Szot, E. Łusakowska, T. Balasubramanian, B. M. Wojek, M. H. Berntsen, O. Tjernberg, and T. Story, *Nat. Mat.* **11**, 1023 (2012).
- ⁵ Y. Tanaka, Z. Ren, T. Sato, K. Nakayama, S. Souma, T. Takahashi, K. Segawa, and Y. Ando, *Nat. Phys.* **8**, 800 (2012).
- ⁶ S.-Y. Xu, C. Liu, N. Alidoust, M. Neupane, D. Qian, I. Belopolski, J.D. Denlinger, Y.J. Wang, H. Lin, L.A. Wray, G. Landolt, B. Slomski, J.H. Dil, A. Marcinkova, E. Morosan, Q. Gibson, R. Sankar, F.C. Chou, R.J. Cava, A. Bansil, and M.Z. Hasan, *Nat. Commun.* **3**, 1192 (2012).
- ⁷ Y. Okada, M. Serbyn, H. Lin, D. Walkup, W. Zhou, C. Dhital, M. Neupane, S. Xu, Y. J. Wang, R. Sankar, F. Chou, A. Bansil, M. Z. Hasan, S. D. Wilson, L. Fu, and V. Madhavan, *Science* **341**, 1496 (2013).
- ⁸ I. Zeljkovic, Y. Okada, M. Serbyn, R. Sankar, D. Walkup, W. Zhou, J. Liu, G. Chang, Y. J. Wang, M. Z. Hasan, F. Chou, H. Lin, A. Bansil, L. Fu, and V. Madhavan, *Nature Mater* **14**, 318 (2015).
- ⁹ T. Nishijima, T. Watanabe, H. Sekiguchi, Y. Ando, E. Shigematsu, R. Ohshima, S. Kuroda, and M. Shiraishi, *Nano Lett.* **23**, 2247 (2023).
- ¹⁰ B.M. Wojek, M.H. Berntsen, V. Jonsson, A. Szczerbakow, P. Dziawa, B.J. Kowalski, T. Story, and O. Tjernberg, *Nat. Commun.* **6**, 8463 (2015).
- ¹¹ B. M. Wojek, P. Dziawa, B. J. Kowalski, A. Szczerbakow, A. M. Black-Schaffer, M. H. Berntsen, T. Balasubramanian, T. Story, and O. Tjernberg, *Phys. Rev. B* **90**, 161202(R) (2014).
- ¹² A. A. Lazarides, C. B. Duke, A. Paton, and A. Kahn, *Phys. Rev. B* **52**, 14895 (1995).
- ¹³ A. Satta and S. de Gironcoli, *Phys. Rev. B* **63**, 033302 (2000).
- ¹⁴ V. L. Deringer and R. Dronskowski, *J.Phys. Chem. C* **120**, 8813, (2016).
- ¹⁵ V.L. Deringer and R. Dronskowski, *ChemPhysChem* **14**, 3108 (2013).
- ¹⁶ S. Sawada and K. Nakamura, *J. Phys. C: Solid State Phys.*, **12**, 1183 (1979).
- ¹⁷ J. Ma, Y. Jia, E. Liang, L. Wu, F. Wang, X. Wang, and X. Hu, *Surface Sci.* **551**, 91 (2003).
- ¹⁸ E. J. W. Verwey, *Rec. Trav. Chim. Pays-Bas* **65**, 521 (1946).
- ¹⁹ C. Yan, J. Liu, Y. Zang, J. Wang, Z. Wang, P. Wang, Z.-D. Zhang, L. Wang, X. Ma, S. Ji, K. He, L. Fu, W. Duan, Q.-K. Xue, and X. Chen *Phys. Rev. Lett.* **112**, 186801 (2014).
- ²⁰ see <http://www.openmx-square.org>
- ²¹ D. M. Ceperley and B. J. Alder, *Phys. Rev. Lett.* **45**, 566 (1980).
- ²² J. P. Perdew and A. Zunger, *Phys. Rev. B* **23**, 5048 (1981).
- ²³ A. Łusakowski, P. Bogusławski, and T. Radzyński, *Phys. Rev. B* **83**, 115206 (2011).
- ²⁴ A. Łusakowski, P. Bogusławski, and T. Story, *Phys. Rev. B* **98**, 125203 (2018).
- ²⁵ T. Kendelewicz, P. Liu, G. E. Brown Jr, and E. J. Nelson, *Surf. Sci.* **395**, 229 (1998).
- ²⁶ K.L.I. Kobayashi, Y. Kato, Y. Katayama, and K.F. Komatsubara, *Phys. Rev. Lett.* **37**, 772 (1976).
- ²⁷ F. Wei, C.-W. Liu, D. Li, C.-Y. Wang, H.-R. Zhang, J.-R. Sun, X. P. A. Gao, S. Ma, and Z. Zhang *PRB* **98**, 161301 (2018)
- ²⁸ J. Tersoff and D. R. Hamann, *Phys. Rev. B* **31**, 805 (1985).
- ²⁹ D. Bassanezi, E.O. Wrasse, and T. M. Schmidt, *Mater. Res. Express* **5**, 015051 (2018).
- ³⁰ P. Bogusławski, Q.-M. Zhang, Z. Zhang, and J. Bernholc, *Phys. Rev. Lett.* **72**, 3694 (1994).
- ³¹ Z. Wang, Q. Liu, J.-W. Luoc, and A. Zunger, *Mater. Horiz.* **6**, 2124 (2019).
- ³² A. Szczerbakow, and H. Berger, *J. Cryst. Growth* **139**, 172 (1994).
- ³³ M. Neupane, S.-Y. Xu, R. Sankar, Q. Gibson, Y. J. Wang, I. Belopolski, N. Alidoust, G. Bian, P. P. Shibayev, D. S. Sanchez, Y. Ohtsubo, A. Taleb-Ibrahimi, S. Basak, W.-F. Tsai, H. Lin, T. Durakiewicz, R. J. Cava, A. Bansil, F. C. Chou, and M. Z. Hasan, *Phys. Rev. B* **92**, 075131 (2015).
- ³⁴ K. Adouby, C. Perez-Vicente, and J.C. Jumas, *Z. Kristallogr.* **213**, 343 (1998).